Paraffin Polydispersity Facilitates Mechanical Gelation

Kristofer Paso,[†] M. Senra,[†] Y. Yi,[‡] A. M. Sastry,[‡] and H. Scott Fogler*,[†]

Department of Chemical Engineering, University of Michigan, Ann Arbor, Michigan 48109, and Department of Mechanical Engineering, University of Michigan, Ann Arbor, Michigan 48109

Incipient wax−oil gel deposits form in crude oil transport pipelines when long-chain *n*-paraffins precipitate at the cold interior surface of the pipe wall. The kinetics of paraffin gel formation was studied using model fluids consisting of monodisperse and polydisperse *n*-paraffin components dissolved in petroleum mineral oil. Classical homogeneous nucleation theory was applied to investigate the supersaturation conditions necessary for crystal formation. Differential scanning calorimetry was used to monitor paraffin crystallization rates and to provide solid-phase fraction measurements. Gelation occurs when growing *n*-paraffin crystals interlock and form a volume-spanning crystal network which entrains the remaining liquid oil among the crystals. Paraffin wax−oil gels exhibit a mechanical response to an imposed oscillatory stress, which is characterized by the elastic storage modulus G′ being greater in magnitude than the viscous loss modulus, G″. Low-temperature rheological gels can form from model fluids with *n*-paraffin contents as low as 0.5 wt %. Images of wax−oil gel morphologies were obtained using a cross-polarized microscope fitted with a z-drive and indicated crystal lengths of ∼10−20 μm. A microstructural gelation model based on percolation theory was introduced to provide predictions of gel formation conditions among randomly oriented paraffin crystals. The structural model provides correlations of crystal morphologies and solid fractions at the percolation threshold condition. Comparison of the initial wax contents required for gelation of monodisperse and polydisperse *n*-paraffin wax indicates that sharp crystal edges and ordered crystal faces hinder the paraffin crystal−crystal "anchoring" interactions which result in mechanical gelation.

1. Introduction

Paraffin deposition and wax plugging are ubiquitous problems faced in cold-environment petroleum production, such as from arctic climates or subsea producing fields. When the temperature of a crude oil or gas condensate fluid drops below the paraffin solubility limit, known as the cloud point, the heaviest *n*-paraffin fractions precipitate out of solution as solid wax crystals. Gelation occurs when paraffin crystals interact to form volume-spanning networks which entrain the remaining liquid oil and impart solidlike mechanical properties to the fluid. In petroleum transport pipelines, paraffin gel deposits form at the cold interior surface of the pipe wall and increase in thickness and hardness with time until, gradually, a complete blockage is formed, at an enormous economic loss to the producer. Successful risk abatement strategies typically incorporate a comprehensive planning and implementation program, utilizing mechanical, thermal, and chemical remediation methods. Proper design of paraffin management systems is dependent upon a priori knowledge of paraffin deposition rates and gel deposit properties. To accurately assess paraffin deposition tendencies, knowledge of pipeline flow characteristics and temperature gradient conditions are required, which are often difficult to reproduce in laboratory settings. A fundamental understanding of the paraffin gelation and deposition process is necessary in order to appropriately scale laboratory deposition rate measurements to field conditions and obtain useful forecasts.

A plethora of investigations have focused on characterizing low-temperature phases and solid−solid transitions of *n*-alkane waxes using X-ray diffraction,[1−5] Raman and IR spectroscopy,[6] and thermal analysis.[7,8] Nucleation studies performed with undiluted single component *n*-paraffins have characterized metastable zone-widths[9] and solid−liquid interfacial energies[10,11] in relation to solid structural phases and surface freezing effects. Polydisperse distributions of *n*-paraffin components dissolved in crude oil[1] or other organic solvents[12,13] assume orthorhombic equilibrium structural phases. Thermodynamic models have been developed which provide accurate predictions of the solid−liquid equilibrium of multicomponent paraffin fluids while accounting for the formation of multiple solid phases due to chain-length variations.[14,15] Solid−liquid-phase equilibria models are useful in establishing the deposition potential of a petroleum fluid on a compositional basis.

Paraffin deposition models have been developed by Singh et al.[16,17] which provide accurate predictions of deposit buildup and aging rates based on pipeline heat- and mass-transfer characteristics. The aging process involves the molecular diffusion of *n*-paraffins from the bulk fluid into the occluded liquid within the deposit, where the paraffin components subsequently precipitate, causing an increase in the solid fraction (and hardness) of the deposit with time.[18] In addition, the influence of shear reduction on the deposition rate has been quantified and applied to predictive deposition models.[19] Lab-scale wax deposition tests using coldfingers[20] or flow loop systems[16] are commonly used to provide forecasts of field deposition and aging rates. To appropriately scale the deposition process and account for effects such as shear reduction and kinetic limita-

* To whom correspondence should be addressed. Tel.: (734) 763-1361. Fax: (734) 763-0459. E-mail: sfogler@umich.edu.
[†] Department of Chemical Engineering.
[‡] Department of Mechanical Engineering.

10.1021/ie050325u CCC: $30.25
Published on Web 08/06/2005

tions, flow conditions must be properly mapped between the laboratory and field systems. Because of the difficulty in establishing pipeline flow patterns in laboratory-scale equipment, predictive deposition models must be sufficiently robust to account for varying shear and temperature-gradient conditions and adhere to fundamental scaling laws.

Singh et al.[21] established the applicability of using superimposed oscillatory rheometric measurements to determine the gelation point of waxy fluids under shear conditions. Paraffin contents of gelled samples in the rheometer provided excellent correlation to measured incipient solid fractions of analogous flow loop deposits for a variety of shear conditions. Venkatesan et al.[22] demonstrated that the rheometric gelation temperature provides a more useful definition of the onset of gelation than the commonly used pour point temperature. The importance of gelation in the wax deposition process has been established by Singh et al.[16,17,21] as well as by Venkatesan et al.[22] Gelation is responsible for the formation of incipient wax deposits in petroleum transport flowlines, as well as for the occlusion of liquid oil at the deposit−fluid interface during deposit growth.

In the work presented here, the role of the kinetics of formation of incipient wax−oil gels is assessed by applying the fundamentals of homogeneous nucleation, crystallization, and gelation theory. Model fluids consisting of *n*-paraffin components dissolved in petroleum mineral oils are formulated in order to provide insight into the crystal−crystal interactions which ultimately lead to gel formation. The experimental methods of differential scanning calorimetry, rheometry, and cross-polarized microscopy provide measures of the crystallization rate, mechanical properties, and crystal morphologies, respectively. One of the primary limitations of current predictive deposition models is the assumption of the complete absence of kinetic limitations in the rates of incipient gel formation and deposit buildup, which allows for the direct application of scaled heat- and mass-transfer correlations based on flow characteristics. Neglecting gelation kinetics considerations may lead to predictions of wax deposition in cases where a stable gel cannot form, resulting in unnecessary capital expenditures related to paraffin remediation and control systems. The current research lays the groundwork for assessing kinetic limitations in paraffin crystallization and gelation rates, which may be applied to existing deposition models and may ultimately result in less conservative wax deposition predictions. The analytical methods developed here using simple model fluids consisting of wax dissolved in mineral oil can be readily extended to the real waxy petroleum fluids encountered in production systems.

2. Experimental Section

2.A. Model Fluids. Wax−oil gels were prepared from model fluids consisting of *n*-paraffin waxes dissolved in mineral oil. The waxes were obtained from Sigma-Aldrich and include a polydisperse wax (mp 65 °C), *n*-C_{36} (mp 75 °C), and *n*-C_{35} (mp 74 °C). The carbon number distribution of the polydisperse wax, analyzed using an Agilent 6890N gas chromatograph with a 0.25 μm fused silica stationary phase and an FID detector, is shown in Figure 1. The mineral oils include Coray-15 lubricating oil obtained from ExxonMobil, as well as a heavy mineral oil obtained from Sigma-Aldrich. Coray-15 exhibits an average molecular weight of 290 and a viscosity at 25 °C of 29 cP, while the heavy mineral oil exhibits an average molecular weight of 424 and a viscosity at 25 °C of 143 cP. Model oils were formulated with either monodisperse or polydisperse *n*-paraffin concentrations ranging from 0.5% to 8% in the mineral oils. Cloud point solubility measurements were performed by heating the samples until a transparent liquid was obtained and subsequently placing the samples in a temperature-controlled water bath for a time period of at least 1 h. Paraffin crystal formation was detected by visual turbidity observation. For each model fluid, the procedure was repeated until the cloud point temperature was determined within an accuracy of ±0.1 °C.

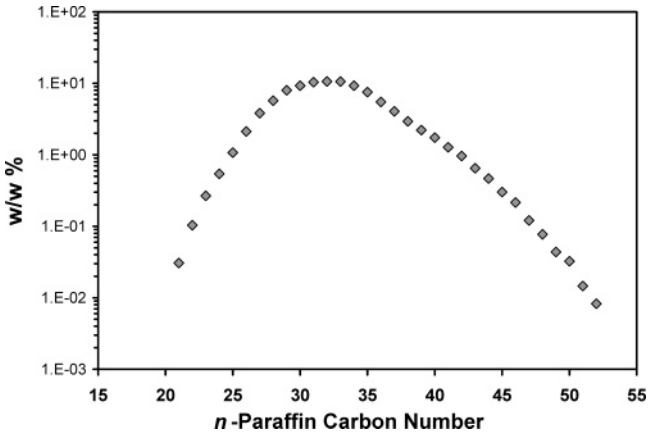

Figure 1. *n*-Paraffin carbon number distribution of the mp 65 °C wax.

2.B. Differential Scanning Calorimetry. Heat flow measurements during cooling were performed using a Perkin-Elmer DSC-7 instrument to monitor crystallization kinetics and provide accurate measures of solid-phase fractions under quiescent conditions. Model fluid samples of at least 25 mg were carefully prepared in aluminum sample pans and weighed. Sample chamber cooling was provided by pumping water through an ice bath, which limits the operating temperature range of the heat flow measurements in accordance with the temperature difference necessary to sustain sample cooling. At cooling rates of 5, 1, and 0.5 °C/min, the lower operating temperature limits are 20, 5.5, and 3.6 °C, respectively. To obtain accurate heat flow measurements, a linear heat capacity baseline was first established by performing a cooling scan with mineral oil in the sample pan. Subsequently, heat flow measurements were performed with the formulated model oils upon sample cooling from a temperature of 70 °C to the lower temperature limit of heat flow detection at rates of 5, 1, and 0.5 °C/min. Nucleation temperatures were obtained by identifying the temperature at which the measured heat flow diverges from the sample heat capacity baseline. The heat flow attributed to crystallization was obtained by subtracting a linear heat capacity interpolation from the measured heat flow. The integrated heat of crystallization was normalized to the appropriate crystallized fraction at the lower temperature limit.

2.C. Rheometry. A controlled stress rheometer (TA Instruments AR1000) was used for the rheological experiments. The instrument was configured with a 4 cm, 1.59° steel cone and equipped with a Peltier plate temperature-control device. During each run, a model fluid sample was contained between the cone and the

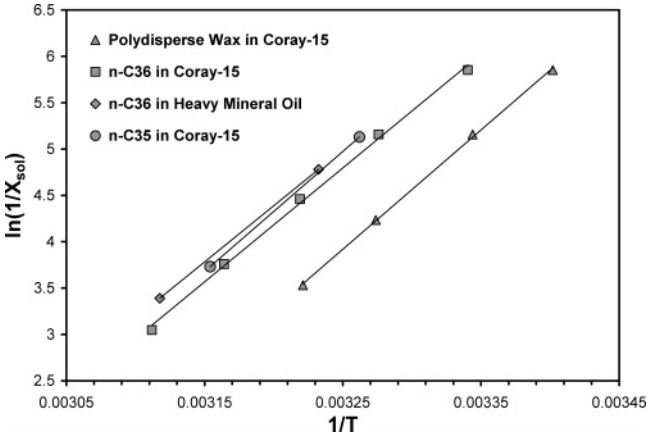

Figure 2. *n*-Paraffin solubilities of monodisperse and polydisperse model fluids, determined from visual cloud point observations.

Peltier plate, and a single-frequency oscillatory stress was imposed upon the sample while the temperature was cooled at a constant rate starting from a temperature of ~10 °C above the respective fluid cloud point. Each rheometric experiment was performed using an oscillatory frequency of 0.1 or 1 Hz and a constant oscillatory stress amplitude within the range of 0.01 to 1 Pa. The mechanical response was characterized by G′, the elastic storage modulus; G″, the dissipative loss modulus; and the oscillatory strain amplitude.

2.D. Cross-Polarized Microscopy. A Nikon Eclipse E600 microscope fitted with a 50X objective lens and equipped with a "*z*-drive" automatic focusing controller was used to obtain 3-D images of the wax−oil gels. Digital images were captured with a Hamamatsu ORCA ER digital camera. The 2-D domain captured in each image represents a rectangular area of 131 × 172 μm. Model oil samples were first cooled at 0.5 °C/min from ~10 °C above the respective fluid cloud point to 10 °C. For the 0.5% polydisperse wax model fluid, the final temperature was reduced to 7.6 °C in order to provide a sufficiently high solid-phase fraction to establish crystal sizes. During the imaging process, the autofocusing controller was synchronized with the digital camera to rapidly obtain 2-D cross-polarized images at 80 focal planes, spaced 1 μm apart, for a total distance in the *z*-direction of 80 μm. Reconstruction software (SimplePCI from Compix, Inc.) was used to create 3-D images from the 2-D *z*-slices by calculating image projections viewed from angles of 0°−360° at 5° intervals. Reconstructed 3-D images can be viewed in continuous rotational mode with the software.

3. Results and Discussion

3.A. Paraffin Solubilities. Paraffin solubilities obtained from cloud point measurements are correlated in Figure 2. The enthalpy and entropy of dissolution are obtained by applying experimental cloud points to the van't Hoff relation[23]

$$\ln\left(\frac{1}{x_{\mathrm{sol}}}\right) = \frac{\Delta H_{\mathrm{dissolution}}}{RT} - \frac{\Delta S_{\mathrm{dissolution}}}{R} \qquad (1)$$

where x_{sol} is the soluble *n*-paraffin mole fraction, $\Delta H_{\mathrm{dissolution}}$ is the dissolution enthalpy (kJ/mol), and $\Delta S_{\mathrm{dissolution}}$ is the dissolution entropy (kJ/mol/K).[23] The van't Hoff relation assumes ideal solubility behavior and a negligible heat capacity change upon crystallization.

Table 1. Paraffin Dissolution Enthalpy (kJ/mol) and Entropy (kJ/mol/K) Values Derived from the Van't Hoff Solubility Relation,[23] Based on Experimental Cloud Points

	polydisperse (Coray-15)	n-C_{36} (Coray-15)	n-C_{36} (heavy oil)	n-C_{35} (Coray-15)
diss. enthalpy	107.1	102.2	100.7	107.6
diss. entropy	0.317	0.292	0.286	0.308

Table 1 shows dissolution enthalpy and entropy values for the paraffin waxes in mineral oil. The van't Hoff relation provides a robust thermodynamic solubility model for single-component *n*-paraffins dissolved in organic solvents at low mass fractions. Dissolution enthalpy and entropy values associated with the n-C_{36} component are nearly independent of the mineral oil viscosity. When the van't Hoff correlation is applied to solubility measurements of polydisperse distributions of *n*-paraffin components in solution, significant uncertainty exists in the $x_{\mathrm{solubility}}$ values because only the highest carbon numbers contribute to the precipitated phase at the initial nucleation point; midrange *n*-paraffin components remain in the liquid phase at the nucleation point. However, if the upper *n*-paraffin fraction which contributes to the first precipitated phase is considered a pseudocomponent in constant proportion to the total *n*-paraffin distribution, the left-hand side of eq 1 can be expressed as $\ln(1/x_{\mathrm{solubility}}) + \ln(1/c)$ for polydisperse *n*-paraffin model fluids. The constant c represents the molar fraction of the wax solute which constitutes the upper pseudocomponent; $x_{\mathrm{solubility}}$ represents solubility measurements based on the initial wax fraction of the model fluid on a molar basis. Application of the pseudocomponent assumption provides an estimate of the dissolution enthalpy of the heaviest paraffin fraction of 107.1 kJ/mol, indicating an average chain length of ~36−38 in the first precipitated phase of the polydisperse wax fluid.

3.B. Classical Homogeneous Nucleation. The supersaturation conditions necessary to induce nucleation are investigated by application of the homogeneous nucleation theory. For simple model fluids consisting of refined paraffins dissolved in mineral oil, the nucleation mechanism is homogeneous. The supersaturation ratio can be expressed as

$$S = \frac{C}{C_{\mathrm{eq}}} \qquad (2)$$

where C represents the *n*-paraffin concentration in solution and C_{eq} represents the equilibrium *n*-paraffin concentration, provided by the van't Hoff solubility theory. Experimental supersaturation values at the nucleation point are obtained by establishing equilibrium paraffin concentrations based on DSC-measured nucleating temperatures. A generalized form of the nucleation rate, applicable to solutions, can be expressed as[24]

$$J = A \exp\left[\frac{-16\pi\sigma^3\nu^2}{3k^3T^3(\ln S)^2}\right] \qquad (3)$$

where σ represents the surface energy of the critical nucleus, ν represents the molecular volume of the nucleating species and is a weak function of temperature, and k represents the Boltzman constant. The preexponential factor A is commonly known as the collision factor and is theoretically related to an equi-

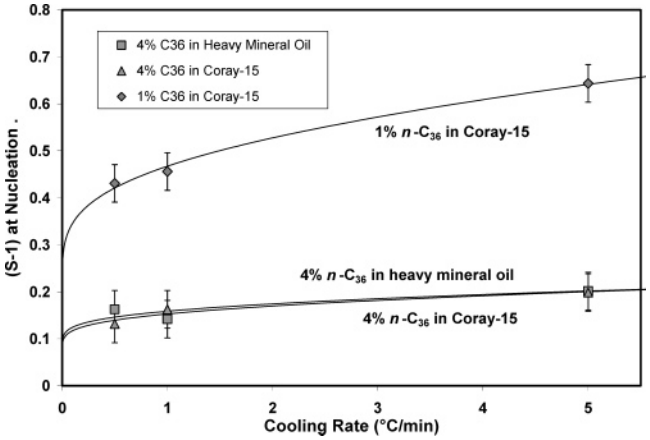

Figure 3. Supersaturation conditions at nucleation for monodisperse model fluids. Solid lines represent homogeneous nucleation theory.

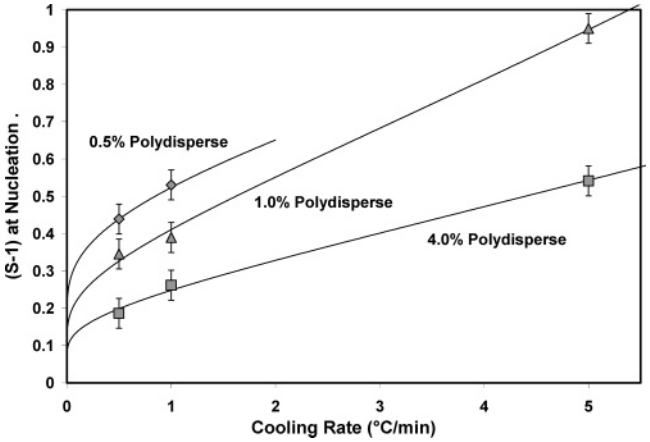

Figure 4. Supersaturation conditions at nucleation for polydisperse wax in Coray-15. Solid lines represent homogeneous nucleation theory.

librium precritical cluster size distribution. When a model paraffin fluid is supercooled under a constant cooling rate, the nucleation rate will increase with time because of the changing temperature and supersaturation conditions. Consequently, to establish the nucleation point dependence upon cooling rate, the nucleation rate expression must be integrated over the nucleation induction time. The integrated nucleation expression yields a nuclei number density.[24]

$$\rho_n = \int_{t_{cp}}^{t_n} J \, dt \tag{4}$$

t_{cp} represents the time at which the sample temperature reaches the cloud point; t_n represents the time at which the sample nucleates. The concept of a critical nuclei number density, ρ_n^*, is established to define the nucleation point within the framework of homogeneous nucleation theory and to facilitate the comparison of experimental nucleation point measurements. Nucleation is assumed to occur when the critical nuclei number density is attained. Integration of the nucleation rate expression is performed by utilizing the van't Hoff solubility relation in the supersaturation term of the exponential denominator. Details of the homogeneous nucleation theory development are provided in the Appendix. Application of the nucleation theory framework to measured nucleation points provides correlated values of σ and A/ρ_n^*.

Figure 3 shows experimental and fitted theoretical supersaturation ratios at the nucleation point for the model fluids consisting of the single component n-C_{36} in mineral oil. Each individual line representing nucleation theory corresponds to specific values of A/ρ_n^* and σ. Hence, A/ρ_n^* and σ depend on the fluid composition. The results indicate that slightly larger supersaturation ratios are necessary to induce nucleation at higher cooling rates. Low initial wax fractions also result in higher supersaturation ratios at the nucleation point. Comparison of supersaturation ratios in the high- and medium-viscosity mineral oils (Figure 3) indicates an absence of transport limitations in the nucleation kinetics. To provide nucleation correlations for the polydisperse model fluids, supersaturation calculations are based on only the pseudocomponent which contributes to the first precipitated fraction, as defined by application of the van't Hoff solubility correlation to measured cloud points. Figure 4 shows experimental and theoretical supersaturation ratios at the nucleation point for

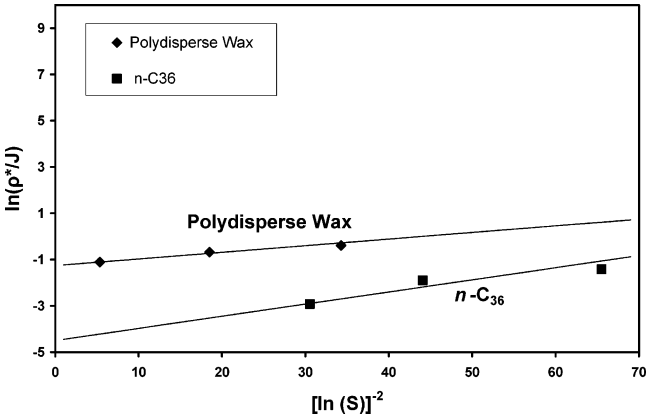

Figure 5. Linearized nucleation rate expression. Solid data points represent theoretical $\ln(\rho^*/J)$ values plotted versus experimental supersaturation ratios.

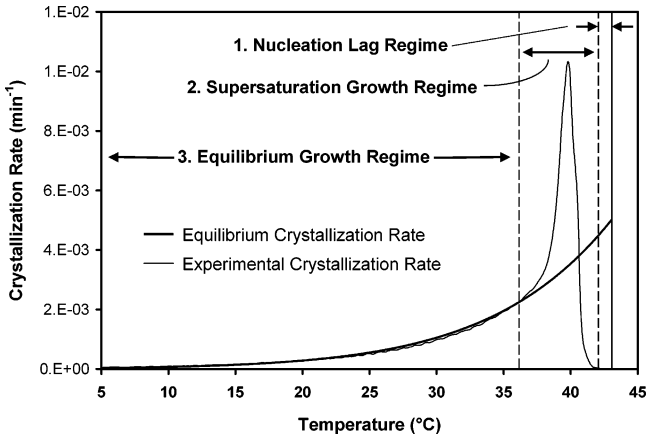

Figure 6. DSC-measured crystallization rate for 4.0% n-C_{36} in Coray-15 at a cooling rate of 1 °C/min. The thick solid curve represents the equilibrium crystallization rate, and the solid vertical line represents the cloud point temperature.

the polydisperse wax in Coray-15. Similar to the case of single-paraffin-component fluids, low initial wax fractions and high cooling rates result in increased supersaturation ratios at nucleation. Optimized surface energy values obtained by fitting the homogeneous nucleation theory expressions to the supersaturation ratios (Figures 3 and 4) measured by DSC (see Figures 6−8) are shown in Table 2. In all cases, surface energies associated with polydisperse paraffin critical nuclei are

Table 2. Fundamental Nucleation Parameters[a]

	0.5% polydisperse wax (Coray-15)	1% polydisperse wax (Coray-15)	4% polydisperse wax (Coray-15)	0.5% n-C_{36} (Coray-15)	1% n-C_{36} (Coray-15)	4% n-C_{36} (Coray-15)	4% n-C_{36} (heavy mineral oil)
T_{cloud} (°C)	20.8	25.9	35.71	26.2	32.1	42.9	47.6
A/ρ_n* (min^{-1})	4.37	2.36	3.53	8.93	29.8	89.8	141.3
σ (dyn/cm)	0.97	0.69	0.50	1.11	1.28	0.66	0.71

[a] Surface energies and A/ρ_n* derived from the nucleation relation expressed in eq 4 applied to experimental nucleation points obtained from DSC measurements.

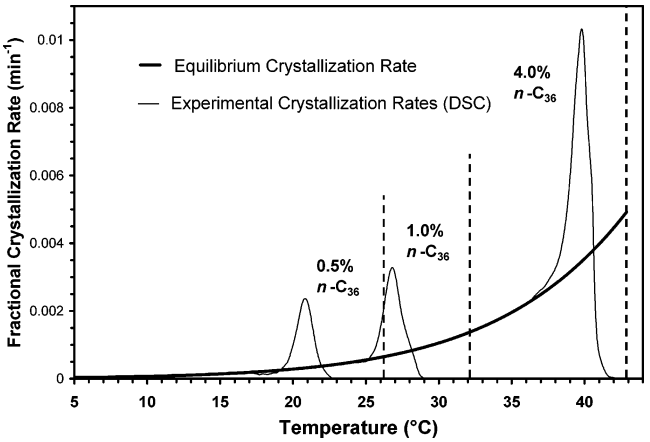

Figure 7. Crystallization rates obtained by DSC for n-C_{36} in Coray-15 at a cooling rate of 1.0 °C/min. The thick solid line represents the equilibrium crystallization rate, and the dashed vertical lines represent the respective cloud point solubility limits.

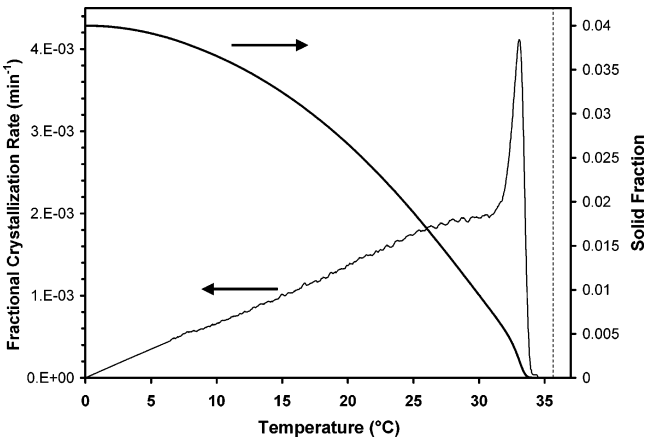

Figure 8. Crystallization rate and solid fraction obtained by DSC for 4% polydisperse wax in Coray-15 at a cooling rate of 1 °C/min. The dashed vertical line represents the cloud point solubility limit.

lower than surface energies of the single-component n-C_{36} critical nuclei. Linearized nucleation rates are shown in Figure 5 for the 4% initial wax fraction fluids.

3.C. Crystallization Kinetics. Paraffin crystallization was investigated at constant cooling rate conditions by DSC heat flow measurements. The enthalpy of fusion relates heat flow to the paraffin crystallization rate. Differences in liquid- and solid-phase heat capacities cause the enthalpy of fusion to vary with temperature according to the following relation

$$\Delta H_{f,i}(T) = \int_T^{T_{m,i}} C_{p,L,i}(T)\,dT + \Delta H_{f,i}(T_{m,i}) + \int_{T_{m,i}}^{T} C_{p,S,i}(T)\,dT \quad (5)$$

where $\Delta H_{f,i}$ represents the enthalpy of fusion of component i, $T_{m,i}$ represents the melting temperature of the pure component i, and $C_{p,L,i}$ and $C_{p,S,i}$ represent the liquid- and solid-phase paraffin heat capacities of the ith component, respectively. The correlations for n-paraffin melting enthalpy (cal/mol) and heat capacity (cal/mol/K) are obtained from Petersen et al.[25] as follows:

$$T_{m,i} = 374.5 + 0.02617MW_i - 20\,171/MW_i \quad (6)$$

$$\Delta H_{f,i} = 0.1426MW_i T_{m,i} \quad (7)$$

$$\Delta C_{p,i}^{L-S}(T) = 0.3033MW_i - (4.635 \times 10^{-4})MW_i T \quad (8)$$

In these correlations, MW_i represents the n-paraffin molecular weight and $\Delta C_{p,i}^{L-S}$ represents the heat capacity difference between the liquid and solid phase of the pure-component paraffin. We will let X represent the mass fraction of paraffin in solution. The experimental crystallization rate, expressed as $-dX/dt$, is obtained by division of the crystallizing heat flow by the enthalpy of fusion and is expressed in terms of mass fraction (of the total wax and oil present) crystallized per minute. Figure 6 shows the experimental crystallization rate for the case of 4% n-C_{36} in Coray-15. Also plotted is the theoretical equilibrium crystallization rate, which is established assuming the complete absence of kinetic limitations in the crystallization rate. The equilibrium crystallization rate, $-dX_s/dt$, is calculated by the following equation using the chain rule of differentiation

$$-\frac{dX_s}{dt} = -\frac{dX_s}{dT}\frac{dT}{dt} \quad (9)$$

The term dX_s/dT is obtained by differentiating the mass fractional form of the van't Hoff equilibrium solubility relation with respect to temperature. The cooling rate is represented by dT/dt. Comparison of experimental and equilibrium crystallization rates indicates three regimes in the crystallization process at low cooling rates. The first regime, starting from high-temperature conditions, is a nucleation lag period, characterized by the onset of supersaturation conditions but without the formation of a solid phase. The second regime, a supersaturation growth period, is driven by the supersaturation established during the nucleation lag period as well as by continuing decreasing solubility conditions. The third regime, an equilibrium growth period, ensues when the supersaturation ratio is diminished and the crystallization rate converges with the equilibrium predictions. The accurate match between experimental and equilibrium crystallization rates in the equilibrium growth regime attests to the robustness of the van't Hoff equilibrium solubility model. Figure 7 shows crystallization rates associated with monodisperse n-C_{36} model fluids of varying paraffin fractions during cooling at 1 °C/min. Because the equilibrium crystallization rate (eq 9) is independent of the initial paraffin fraction, a single master equilibrium crystallization curve applies to all initial paraffin fractions at a particular cooling rate. In each case, the nucleation lag period results in a super-

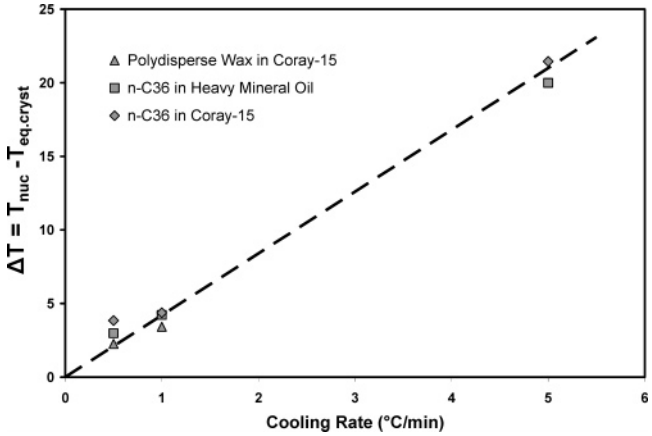

Figure 9. Temperature widths of the supersaturation cooling regime for polydisperse and monodisperse model fluids of 4% initial wax fraction. The fitted line corresponds to a supersaturation regime time span of 4.2 min.

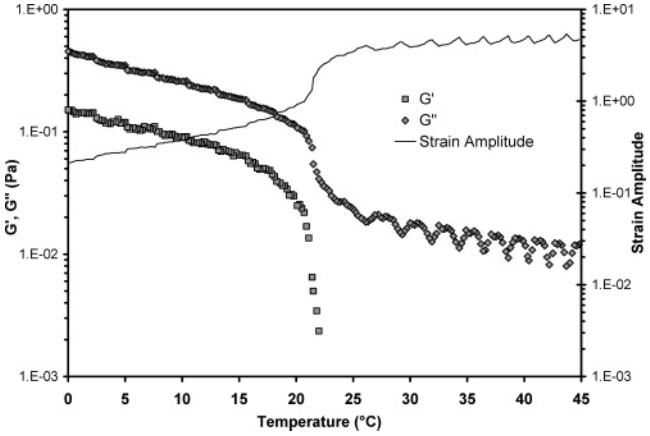

Figure 10. Mechanical response of 0.5% n-C_{36} in Coray-15 resulting from an imposed oscillatory shear stress of 0.1 Pa at a frequency of 0.1 Hz (cooling rate = 0.5 °C/min).

saturation growth period in which the crystallization rate temporarily spikes well above the equilibrium crystallization rate. Subsequently, the crystallization rate converges with the equilibrium crystallization rate predicted by the van't Hoff relation.

Figure 8 shows the crystallization rate of the 4% polydisperse wax in Coray-15 at a cooling rate of 1 °C/min. A nucleation lag period and a supersaturation growth regime are clearly evident in the high-temperature range. Because of the broad distribution of n-paraffin components in the polydisperse wax model fluid, the equilibrium crystallization rate does not exhibit an exponential profile as in the monodisperse case. Instead, the total crystallization rate reflects a sum of crystallization rates associated with a range of n-paraffin components and exhibits a nearly linear profile in the low-temperature range. The abundant presence of n-paraffin carbon number components in the mid-20s shifts a large fraction of the crystallization activity to low single digit temperatures, below the operating limits of the DSC instrument. Therefore, for the polydisperse wax model fluids, the low-temperature crystallization rates are linearly extrapolated to zero in order to provide a closed form integral for solid fraction determination. Calculated solid-phase fractions of monodisperse and polydisperse wax model fluids are applied in gelation correlations.

When comparing measured crystallization profiles with the master equilibrium crystallization rate curve shown in Figure 7, it is evident that the crystallization peaks are a result of the supersaturation generated during the nucleation lag regime. Therefore, at low cooling rate conditions, homogeneous nucleation limitations represent the primary deviation of real crystallization rates from equilibrium crystallization rate predictions. Within the supersaturation growth regime, the crystallization rate is limited by the rate of paraffin chain addition to the growing crystal faces. The duration of the supersaturation growth regime is established by defining the temperature span of the supersaturation growth regime as $\Delta T = T_{\mathrm{nuc}} - T_{\mathrm{eq.cryst}}$, where $T_{\mathrm{eq.cryst}}$ denotes the temperature at which the crystallization rate converges with the equilibrium crystallization rate prediction. Figure 9 shows supersaturation growth regime ΔT widths for the 4% n-C_{36} and 4% polydisperse wax model fluids. The ΔT temperature span of the supersaturation growth regime follows a linear dependence upon cooling rate, reflecting a constant supersaturation growth time of ~4.2 min before equilibrium crystallization is achieved. The ΔT temperature span of the supersaturation growth regime is independent of the model fluid viscosity, providing evidence of the absence of transport limitations in the crystallization rate.

3.D. Gelation Kinetics. Changes in the mechanical properties of waxy model fluids were investigated at constant cooling rate conditions by using controlled-stress rheometric measurements. To characterize the mechanical properties of model fluids during the gelation process, an oscillatory stress is imposed upon the fluid sample. In general, mechanically weak gels, formed from low wax-content fluids, require a smaller imposed oscillatory stress amplitude in order to obtain a quantifiable mechanical response. An imposed oscillatory stress amplitude of 0.1 Pa at a frequency of 0.1 Hz was sufficient to monitor the mechanical response during cooling of all Coray-15-based model fluids with the exception of the 4% polydisperse wax model fluid. At the midrange cooling rates of 1 and 2 °C/min for the 4% polydisperse wax fluid, the characteristic time associated with the initial strain amplitude reduction interferes with the oscillatory periodicity of the imposed stress, resulting in unquantifiable G′ and G″ values near the gel point. Therefore, to obtain a quantifiable mechanical response, an imposed oscillatory stress amplitude of 1 Pa at a frequency of 1 Hz was utilized at the midrange cooling rates for the 4% polydisperse wax fluid.

When the fluid temperature is maintained above the cloud point, a Newtonian mechanical response is obtained, characterized by a finite value of the viscous loss modulus, G″. After the initial nucleation event, the presence of solid paraffin crystals causes an increase in the viscosity of the model fluid, resulting in increased values of the measured loss modulus, G″. The formation of random interaction networks among the growing paraffin crystals imparts a solidlike mechanical response to the fluid, which is characterized by finite values of the elastic storage modulus, G′. Figure 10 shows changes in the mechanical moduli and oscillatory strain amplitude associated with paraffin crystallization in the 0.5% n-C_{36}/Coray-15 model fluid at a cooling rate of 0.5 °C/min. At temperatures below the fluid cloud point of 26.1 °C, an increase is observed in the viscous loss modulus, G″, which correlates to a decrease in the oscillatory strain amplitude. The formation of crystal−

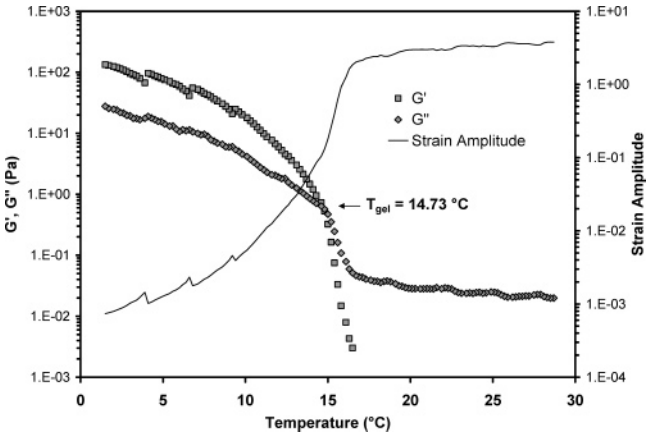

Figure 11. Mechanical response of 0.5% polydisperse wax in Coray-15 resulting from an imposed oscillatory shear stress of 0.1 Pa at a frequency of 0.1 Hz (cooling rate = 0.5 °C/min).

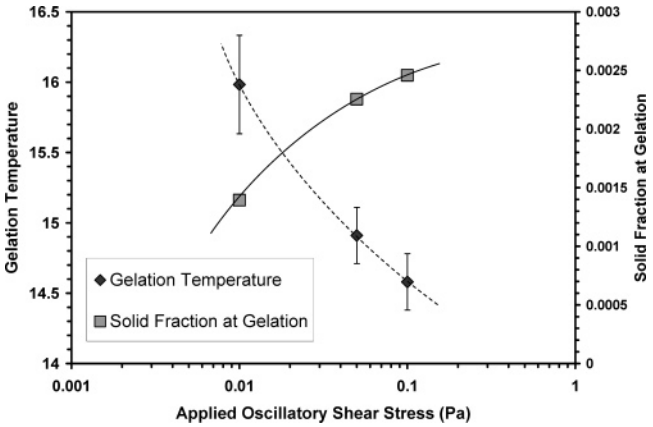

Figure 12. Gel point temperatures and correlated solid fractions for 0.5% polydisperse wax in Coray-15 at a frequency of 0.1 Hz for varying shear stress amplitudes (cooling rate = 0.5 °C/min).

crystal interactions is detected at temperatures below 22.3 °C by finite values of the elastic storage modulus, G′. As the temperature is further lowered, the degree of interaction among the wax crystals increases, which is reflected in an increase in the storage modulus G′. However, the value of the elastic storage modulus does not exceed the value of the loss modulus, indicating the absence of a volume-spanning crystal network. The sample behaves as a viscous fluid with a small degree of elasticity at low temperatures.

Figure 11 shows rheometric data of the 0.5% polydisperse wax in Coray-15 sample obtained at a cooling rate of 0.5 °C/min. A crossover in the values of G′ and G″ occurs at an interpolated temperature of 14.73 °C, defining the experimental gelation temperature of the fluid and confirming the formation of a continuous paraffin crystal interaction network. The reduction in oscillatory strain amplitude associated with cooling the polydisperse wax fluid from above the cloud point to ~0 °C is ~3 orders of magnitude, confirming the gellike mechanical properties of the polydisperse paraffin model fluid at low temperatures. The strain amplitude reduction of the analogous monodisperse n-C_{36} model fluid (Figure 10) is ~1 order of magnitude and is primarily a result of the viscosity increase associated with crystallization.

Rheometric gelation temperatures were established at cooling rates ranging from 0.5 to 5 °C/min for the model fluids consisting of n-C_{35}, n-C_{36}, and the polydisperse n-paraffin wax in Coray-15. The gel point temperature exhibits a dependency upon the imposed oscillatory stress amplitude, as shown in Figure 12 for the 0.5% polydisperse wax fluid. An increase in the oscillatory stress amplitude from 0.01 to 0.1 Pa at a frequency of 0.1 Hz causes a 1.4 °C depression in the experimental gel point temperature, demonstrating that gel point temperatures obtained at dissimilar imposed stress conditions cannot be directly compared. The gel temperature reduction indicates a shear degradation effect on the gel structure, in which the imposed stress hinders the formation of a volume-spanning crystal network. When a paraffin crystal network begins to form under an imposed stress, the occluded liquid is unable to bear a mechanical load, and the applied stress is localized to the low-density crystal linkages. A sample-spanning network of crystal interactions cannot form unless the density of crystal linkages is sufficient to sustain the maximum mechanical load associated with the applied oscillatory stress. When a higher stress is imposed upon the sample during the gelation process, a higher density of crystal linkages is necessary to sustain the applied stress and provide a gellike mechanical response. Hence, when the imposed oscillatory stress amplitude increases, the gel point is depressed to lower temperatures corresponding to larger solid fractions. Figure 12 shows experimental gel point solid fractions for the 0.5% polydisperse wax fluid, confirming that larger solid fractions are necessary to gel model waxy fluids under higher imposed oscillatory stress conditions.

To facilitate comparison of gel point temperatures obtained under the dissimilar frequency and stress amplitude conditions for the 4% polydisperse wax model fluid, a correction is established to account for the gel temperature depression effect of changing the rheometric conditions from 0.1 Pa and 0.1 Hz to 1 Pa and 1 Hz. At the higher stress conditions, experimental gel point temperatures are reduced by 0.5 and 0.67 °C at cooling rates of 0.5 and 5 °C/min, respectively. Applying a linear interpolation to the gel temperature reductions between 0.5 °C and 5 °C, gel temperature reductions of 0.52 and 0.56 °C are predicted for cooling rate conditions of 1 and 2 °C/min, respectively. The corrections for the gel temperature depression effect are applied to the gel point temperatures obtained at the higher stress and frequency conditions, such that gel temperature correlations remain consistent with the imposed 0.1 Pa and 0.1 Hz rheometric condition.

Figure 13 shows gelation temperature dependencies upon cooling rate for the polydisperse model fluids consisting of 0.5, 1, and 4 wt % of paraffin in Coray-15. Experimental gel point temperatures decrease with increasing cooling rate; a stronger cooling rate dependence is exhibited at lower initial wax fractions. The offset in gel point temperatures of the various paraffin weight fraction fluids correlates to solubility differences. Figure 14 shows gel point temperatures of the monodisperse paraffin fluids consisting of 1% and 4% weight fractions of n-C_{35} and n-C_{36} in Coray-15 mineral oil. Stronger cooling rate dependencies are observed for the n-C_{36} fluids than for the n-C_{35} fluids, indicating a stronger time-dependency in the formation of the crystal interaction network of the n-C_{36} paraffin fluid. For the 0.5% n-C_{36} fluid, no crossover in G′ and G″ values was observed at any cooling rate. For the 0.5% n-C_{35} fluid, no crossover in G′ and G″ values was observed at 0.5 °C/min, although poorly reproducible gel point temper-

Table 3. Solid Fraction Estimates at the Incipient Gel Point Temperature[a]

cooling rate (°C/min)	0.5% polydisperse wax	1% polydisperse wax	4% polydisperse wax	1% n-C_{36}	4% n-C_{36}	1% n-C_{35}	4% n-C_{35}
0.5	0.0028	0.0025	0.0018	0.0060	8.4×10^{-5}	0.0050	4.5×10^{-4}
1	0.0008	0.0017	0.0009	0.0075	0.005	0.0054	3.5×10^{-4}
2	N/A	N/A	N/A	0.0095	0.019	0.0044	8.8×10^{-4}
5	N/A	N/A	N/A	0.0095	0.031	0.0098	0.0058

[a] Gel point temperatures which are out of range of DSC solid fraction measurements are denoted by N/A.

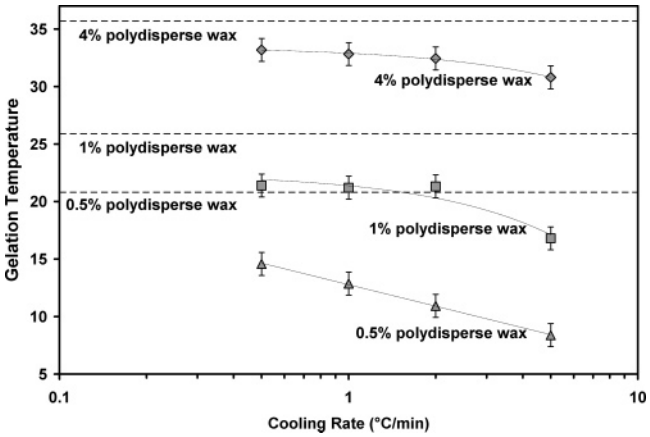

Figure 13. Experimental gelation temperatures for polydisperse model fluids. The dashed horizontal lines represent the respective cloud point solubility limits.

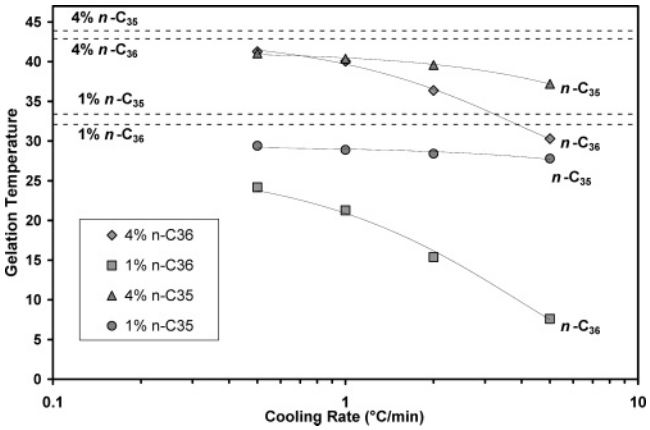

Figure 14. Experimental gelation temperatures for monodisperse model fluids. Cloud point temperatures are indicated by the dashed horizontal lines.

atures were obtained at higher cooling rates. The poor reproducibility is a result of the fragile gel structure as well as the finite sample volume of the rheometer.

Gelation temperatures obtained from the controlled-stress rheometric measurements are correlated with solid fractions obtained by integration of DSC-measured crystallization rates, providing qualitative correlations of the solid-phase fraction at the gelation temperature. Table 3 provides incipient solid-fraction estimates of monodisperse n-C_{36} and n-C_{35} as well as polydisperse model fluids. The large dependence of incipient gel solid fractions upon cooling rate for the 4% monodisperse n-C_{36} and n-C_{35} cases is an indication of time-dependency in the crystal aggregation and network formation. The even carbon number n-C_{36} paraffin exhibits a stronger time-dependency than that of the odd carbon number n-C_{35}. In the case of the polydisperse wax fluids, the observed reductions in incipient gel solid fraction with increasing cooling rate result from the shear degradation effect. At the lower cooling rate, 0.5 °C/min, the imposed shear degrades the crystal network structure for a longer time duration during the gelation process, requiring an increased solid fraction at the incipient gel point in order to obtain a volume-spanning crystal network. The results suggest that fundamental differences exist in the morphology and/or structural dynamics of monodisperse and polydisperse n-paraffin wax−oil gels. To investigate the microstructural mechanism of gelation, cross-polarized images are obtained of the wax−oil gels.

3.E. Cross-Polarized Imaging. The 3-D images seen on the computer by rotating the sample are difficult to see in 2-D. Consequently, the description that follows will contain information that is difficult to deduce from Figure 15. Figure 15a shows a composite image of 0.5% n-C_{36} in Coray-15 at a temperature of 10 °C, corresponding to a DSC-measured solid fraction of 0.47%, indicating nearly complete crystallization of the added n-paraffin. The image is obtained by reconstruction of the 80 single z-slice images spaced at 1 μm intervals, calculated about a rotational angle of 0°. The crystals which are visible in the 0° composite image are positioned at varying z-depths in the 3-D sample domain. The monodisperse crystals depicted in Figure 15a are randomly oriented and exhibit minimal crystal−crystal interaction, which is confirmed by rheometric measurements indicating the elastic storage modulus is of lower magnitude than the viscous loss modulus throughout the entire temperature range. A small curvature in the crystal faces is evident for the monodisperse n-C_{36} crystals, which is the result of dislocations in the lamellar structure of the solid phase.

Figure 15b shows a 0° rotation composite image of the 0.5% polydisperse wax in Coray-15 at a temperature of 7.6 °C, corresponding to a DSC-determined solid-phase fraction of 0.44%, indicating nearly complete crystallization. Correlated rheometric measurements indicate a gellike mechanical response at temperatures below 14.58 °C. The polydisperse crystals appear to exhibit less separation than the monodisperse crystals. Image analysis results shown in Table 4 indicate a smaller average crystal length and width of the polydisperse crystals compared to the monodisperse crystals of 0.5% initial wax fraction. Figure 15c shows a 0° rotation composite image of the 4% polydisperse wax in Coray-15 at a temperature of 10 °C, corresponding to a DSC-determined solid-phase fraction of 3.66% and a gellike mechanical response. The formation of a volume-spanning crystal network which results in mechanical gelation is clearly evident from the composite image. Because of the difficulties in representing reconstructed 3-D wax crystal images, a 2-D schematic of the crystal orientation concepts is provided based on observations of the crystal images in continuous rotational mode. Figure 16a represents the condition in which paraffin crystals have formed in solution, but maintain minimal crystal−crystal interaction, such as exhibited by the monodisperse crystals. Conversely,

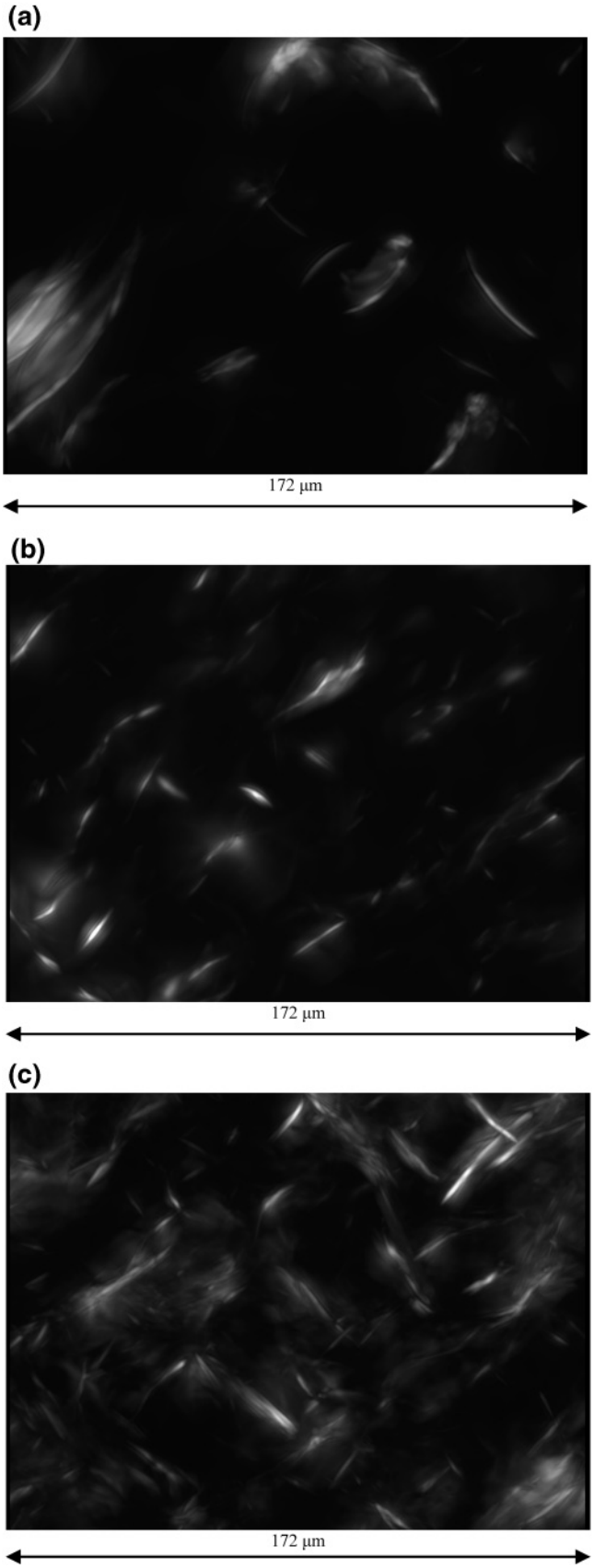

Figure 15. A composite image obtained using a cross-polarized microscope fitted with a 50X objective lens of (a) 0.5% n-C_{36} in Coray-15, (b) 0.5% polydisperse wax in Coray-15, (c) 4% polydisperse wax in Coray-15.

Figure 16b represents a volume-spanning crystal interaction network which forms a strong gel and entrains the remaining liquid oil within the crystal structure, as exhibited by the polydisperse crystals.

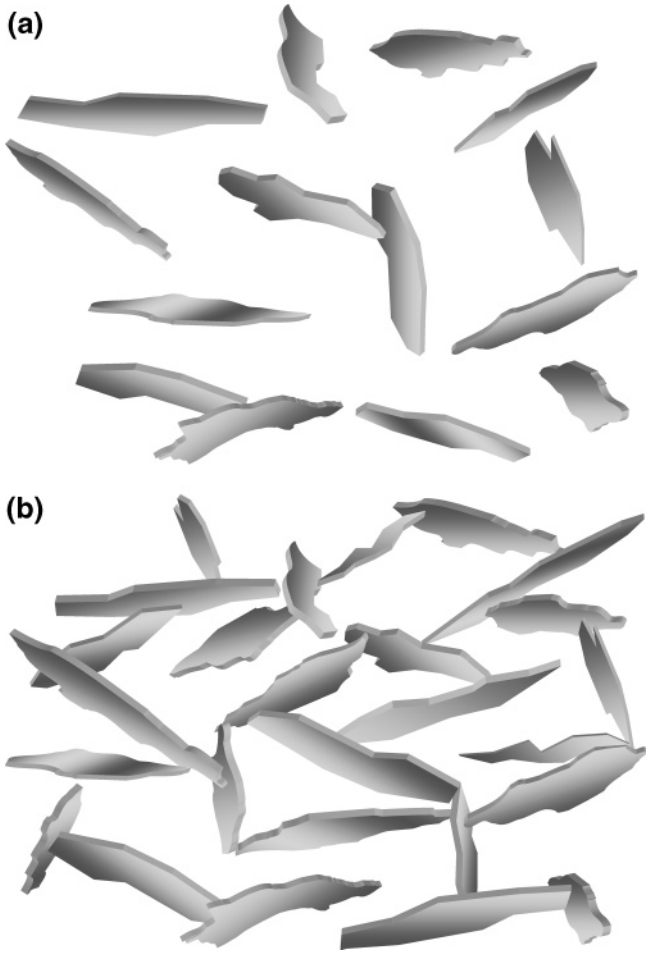

Figure 16. (a) An artist's rendition from 3-D images of free crystals in solution. The crystals do not form a volume-spanning crystal interaction network. (b) An artist's rendition from 3-D images of physical gelation by paraffin crystals. The crystals form a volume-spanning crystal interaction network.

Several limitations are inherent to the use of cross-polarized imaging in determining n-paraffin crystal dimensions. Although 2-D z-slice images are obtained at single focal planes spaced at 1 μm intervals, the rotated polarized light intensity originating from a crystalline particle is projected across several focal planes. Higher intensity images are projected across an increased number of focal planes, producing diffuse shadow images in the z-direction of the originating particle. Hence, the sharpest 2-D composite crystal images are obtained at 0° rotation angles where the diffuse shadow images are concealed by genuine crystal images. Light intensity projection in the z-direction results in distortion of crystal dimensions. For crystal orientations in which the primary crystal face normal vector is parallel to the focal plane, a high intensity of rotated polarized light is produced because of crystal alignment with the source illumination. The high polarized light intensity correlates to an apparent elongation of the crystal in the z-dimension. Paraffin crystals oriented such that the primary crystal face normal vector forms an angle with the focal plane exhibit distortions in apparent crystal width as well as in z-dimension length. Light intensity projected across adjacent focal planes increases the illumination width associated with the in-focal-plane crystal position. Hence,

Table 4. Paraffin Crystal Dimensions Obtained by Averaging the 2-D Image Analysis Results of 80 *z*-Slices (1 μm Intervals) of Each Sample

	solid fraction (DSC)	length mean (μm)	thickness mean (μm)	maximum aspect ratio	minimum aspect ratio	mean aspect ratio
0.5% polydisperse	0.0044	7.55	1.94	3.62	1.99	3.24
0.5% *n*-C_{36}	0.0047	9.9	3.22	11.83	2.82	3.81
1% polydisperse	0.0083	8.78	2.27	4.35	2.95	3.49
1% *n*-C_{36}	0.0095	7.06	2.28	3.48	2.44	2.75
4% polydisperse	0.0366	6.73	2.12	2.42	1.56	2.2
4% *n*-C_{36}	0.0395	7.99	3.01	2.6	2.15	2.47

the image analysis crystal aspect ratios provided in Table 4 do not reflect accurate crystal dimensions.

Paraffin birefringence properties favor illumination of crystals oriented such that the in-plane component of the crystal face normal vector forms a 45° angle with either the *x*-axis or *y*-axis of the focal plane. Paraffin crystals aligned vertically or horizontally in the *x*−*y* plane are not captured by cross-polarized imaging techniques. Hence, exact measures of crystal lengths are not provided by standard image analysis of luminescent domains in 2-D cross-polarized images. Instead, the upper bound to the range of crystal lengths observed in a cross-polarized image may provide a more accurate estimate of the primary crystal dimension. Orientational imaging effects must be considered when correlating experimental gelation conditions with percolation theory predictions.

3.F. Percolation Theory Application. To provide fundamental insight into the structures and morphologies of wax−oil gels formed from randomly nucleated wax crystals, an extension is made to an established three-dimensional analytical percolation approximation and is applied to wax−oil gel systems. The percolation threshold is considered to be the fractional volume of the solid crystalline phase at which it forms a continuous, domain-spanning path connected by crystal−crystal interactions. Robust three-dimensional percolation threshold points have been established for only a few simple particle geometries.[26] Geometric assumptions must be made concerning paraffin crystal morphologies in order to utilize percolation predictions for wax−oil gels. In this work, ellipsoidal geometries with primary axis R_1, R_2, and R_3 are used to represent paraffin crystals, as shown in Figure 17. If the two longest primary axes are equal in length, the geometry is an oblate spheroid. Conceptually, the ellipsoid geometries are rotated about their origin in order to map out the spherical rotational volume of interaction.[27] Thus, the paraffin crystals are treated as spherical particle domains, which allow the use of spherical percolation threshold models to predict gelation conditions. Figure 18 shows a visual representation of the "crystal interaction volume" concept used in applying the percolation thresholds. Theoretical gelation is equated to the condition of an unbounded spherical interaction network. An analytical percolation threshold for randomly oriented uniform overlapping spheres[26] of 0.295 is used to obtain gelation correlations. Implementation of the crystal interaction volume for ellipsoid geometries provides the following prediction of the solid-phase fraction necessary for theoretical gelation:

$$\phi_g = \theta_p \frac{1}{\alpha_1}\frac{1}{\alpha_2} \tag{10}$$

In this relation, ϕ_g represents the solid-phase fraction at the percolation threshold, $\theta_p = 0.295$ represents the spherical percolation threshold, and α_1 and α_2 represent the primary and secondary ellipsoidal aspect ratios.

Morphological and orientational assumptions must be made concerning individual crystals in order to provide insightful correlations between percolation theory and crystal morphologies in the gel. Application of the spheroid (i.e., $\alpha_2 = 1$) approximation to paraffin crystals allows the crystal length to be established as the maximum individual 2-D crystal lengths observed in the cross-polarized images, circumventing distortions associated with shadow image projection in the *z*-direction. In addition, it is assumed that paraffin crystals oriented at 45° in the *x*−*y* focal plane are representative of the paraffin crystals which contribute to the percolation structure of the wax−oil gel.

The image in Figure 15b represents a 0.44% solid-fraction polydisperse paraffin gel with maximum single-crystal lengths (at 45° orientation) of ~16 μm. Application of percolation theory yields a spheroid primary aspect ratio, α_1, of 67, corresponding to a mean crystal thickness of ~0.24 μm and a crystal number density of

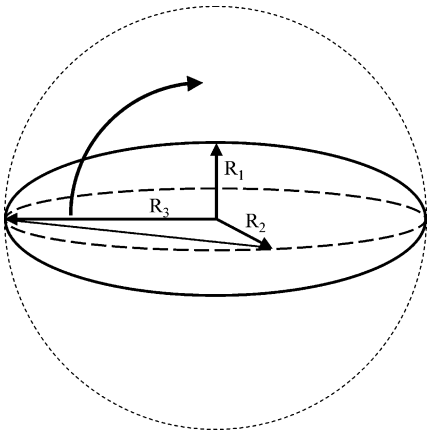

Figure 17. A pictorial representation of the "crystal interaction volume" concept. Ellipsoid geometries are utilized to represent paraffin crystals.

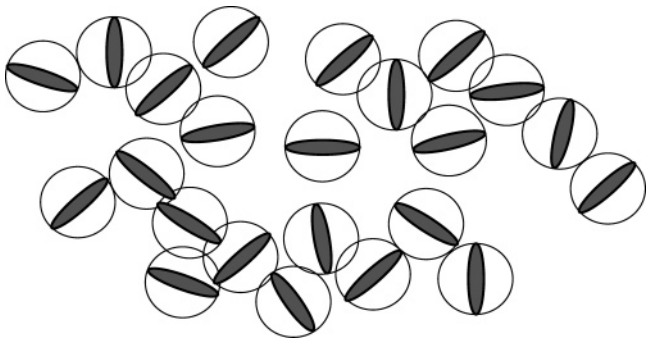

Figure 18. A visual representation of the "crystal interaction volume" concept for randomly oriented paraffin crystals. A 3-D spherical percolation threshold of 0.295 is utilized in the gelation model.

1.11×10^4 mm^{-3}. By comparison, maximum monodisperse n-C_{36} single-crystal lengths are ~25 μm, corresponding to a spheroid primary aspect ratio of 29, a mean crystal thickness of ~0.86 μm, and a crystal number density of 0.27×10^4 mm^{-3}.

Percolation prediction correlations are ideal theoretical constructs that are independent of crystal−crystal interaction dynamics. As such, percolation is a necessary but not sufficient condition for gelation. The formation of a crystal percolation network will lead to gelation only if the number density and strength of the crystal−crystal interactions are sufficient to impart solidlike properties to the fluid. Evidence exists that crystal surface properties influence wax−oil gel strengths. Imia et al.[28] have demonstrated that smooth crystal surfaces associated with monodisperse n-C_{32} crystals form mechanically weak gels; increased gel strengths were obtained by mixing two paraffin chain lengths (n-C_{30} and n-C_{32}) to induce lamellar surface structure disorder. It is mechanistically consistent that sharp crystal edges and smooth crystal faces associated with monodisperse n-paraffin crystals provide a smaller area of interaction between crystal faces and edges, resulting in weaker crystal−crystal "anchoring" interactions.

Percolation threshold theory provides direct gelation condition predictions only in the limit of ideal crystal−crystal anchoring interactions, in which rigid solid−solid interactions dominate the fluid mechanical response. For gelation to occur in fluids with weak crystal−crystal interactions, a larger number density of interaction sites is necessary to compensate for the weaker interactions, necessitating an increased solid fraction at the gelation point. Because strong crystal−crystal interactions are dependent upon the polydispersity of the solid-phase n-paraffin, a larger crystal number density (and solid fraction) is required for gelation to occur in monodisperse paraffin fluids with weak crystal−crystal interactions. Hence, a gel is able to form from the 0.5% polydisperse wax fluid, while the monodisperse n-C_{35} and n-C_{36} fluids require a 1% paraffin content in order to form coherent gels, indicating that the interaction volume for the monodisperse fluid must be significantly greater than the percolation threshold fraction in order to induce gelation. Therefore, the theoretically correlated monodisperse crystal aspect ratio of 29 underpredicts the real aspect ratio of the crystals, which may exhibit values closer to those of the polydisperse paraffin crystals.

Beyond the morphological ambiguities associated with crystal imaging and percolation threshold application, it is clear that polydispersity in the n-paraffin composition of a model petroleum fluid facilitates gelation by a reduction in the surface energy of the critical nuclei, resulting in higher nucleation rates and increased crystal number densities, as well as providing surface roughness to paraffin crystals on a nanometer scale, facilitating strong crystal−crystal interactions of London van der Waals forces.

4. Conclusions

Application of the van't Hoff solubility model within the framework of classical homogeneous nucleation theory demonstrates conclusively that nucleation represents the primary kinetic limitation associated with crystallization of n-paraffins in organic solution at low cooling rate conditions. Crystallization rate limitations become significant at high cooling rates. The introduction of chain-length variations effects a reduction in the critical nucleus surface energy via cocrystallization of dissimilar chain-length paraffins. The initial nucleation event is dependent upon the solubility behavior of the highest fraction of n-paraffin components in a fluid, which can be readily established using a pseudocomponent analysis based on cloud point measurements. In a real petroleum fluid with a broad carbon number distribution, the majority of n-paraffin components will crystallize in the equilibrium cooling regime at low cooling rate conditions.

London van der Waals interactions between paraffin crystals in model waxy petroleum fluids result in drastic changes in mechanical properties at low temperatures. Model fluids consisting of n-paraffin components dissolved in mineral oil exhibit a low-temperature gellike mechanical response to an imposed low-frequency oscillatory stress. The gel point of a waxy model petroleum fluid is dependent on the morphologies and surface characteristics of the randomly oriented paraffin crystals. Paraffin crystals composed of a single-chain-length component exhibit ordered surfaces and sharp edges, providing minimal crystal−crystal contact and weak interactions. Polydisperse n-paraffin crystals exhibit nanoscale surface roughness which provides contact "mesh" points for strong crystal−crystal interactions, allowing mechanical gelation at smaller wax contents. Percolation threshold models provide accurate gel point predictions for physical gelation systems which exhibit strong particle−particle interactions, while underpredicting the solid fraction necessary to induce gelation in weakly interacting particles systems. The inherent n-paraffin polydispersity of real petroleum fluids ensures that a mechanically strong gel may form from nearly any paraffinic fluid at a sufficiently low temperature.

This work demonstrates the importance of considering nucleation effects in the rate of incipient gel formation. In pipeline systems where the bulk fluid temperature is maintained at a temperature above the fluid cloud point, nucleation may be a significant factor in the crystallization kinetics and may occur via a homogeneous or heterogeneous mechanism depending upon the content of the fluid. Advancements in computational fluid dynamics of wax deposition should incorporate nucleation theory to accurately predict rates of incipient paraffin gel formation.

Acknowledgment

The authors wish to acknowledge financial support from the following members of the University of Michigan Industrial Affiliates Program: Baker Petrolite, ChevronTexaco, ConocoPhillips, Shell Oil, Schlumberger, and Total.

Appendix

As a thermodynamic framework for the calculation of the critical nucleus surface energy, we use the van't Hoff solubility theory, assuming ideal mixing in the liquid phase and a negligible heat capacity change upon crystallization. Application of the supersaturation definition in mole fraction yields the following functionality for the logarithm of the supersaturation ratio

$$\ln(S) = \frac{\Delta H}{R}\left(\frac{1}{T} - \frac{1}{T_{\text{cloud}}}\right)$$

which can be rewritten as

$$\ln(S) = \frac{1}{kT}\left(\frac{\Delta H}{N_A}\right)\left(\frac{T_c - T}{T_c}\right)$$

where $R = kN_A$. Insertion into the nucleation rate expression, eq 3, yields

$$J = A \exp\left[\frac{-16\pi\sigma^3\nu^2}{3kT\left(\frac{\Delta H}{N_A T_c}\right)^2 (T_c - T)^2}\right]$$

The temperature dependencies exhibited in the denominator are $T(T_c - T)^2$. A Taylor expansion about T_c yields the following exact relationship for the temperature dependencies in the denominator:

$$T(T_c - T)^2 = T_c(T_c - T)^2 - (T_c - T)^3$$

A comparison of terms with the incorporated experimental nucleation point temperatures confirms that the second term represents <1.5% of the total value for all nucleation conditions. Application of the first-term Taylor approximation, as well as constant cooling rate conditions, such that $\Delta T = (T_c - T) = R_c t$ (where R_c represents the cooling rate and t represents time), results in the following expression for the integrated nucleation rate:

$$\int_{t=0}^{t=t_{nuc}} A \exp\left(\frac{-16\pi\sigma^3\nu^2}{3kT_c^{-1}\left(\frac{\Delta H}{N_A}\right)^2 R_c^{\,2} t^2}\right) dt = \rho_n^*$$

An analytical solution to the integral is obtained where

$$B = \frac{16\pi\sigma^3\nu^2}{3kT_e^{-1}\left(\frac{\Delta H}{N_A}\right)^2}$$

using the following definite integral

$$\int_{x=0}^{x=X} \exp\left(\frac{-\alpha}{x^2}\right) dx = \exp\left(\frac{-\alpha}{X^2}\right)X - \sqrt{\alpha\pi}\,\mathrm{erfc}\left(\frac{\sqrt{\alpha}}{X}\right)$$

such that

$$A \exp\left(\frac{-B/R^2}{t_{nuc}^{\,2}}\right)t_{nuc} - A\sqrt{\frac{B\pi}{R^2}}\,\mathrm{erfc}\left(\frac{\sqrt{B/R^2}}{t_{nuc}}\right) = \rho^*$$

Applying the definition of ΔT, the relationship can be expressed as

$$\left(\frac{A}{\rho^*}\right)\Delta T_{nuc}\left[\exp\left(\frac{-B}{\Delta T_{nuc}^{\,2}}\right) - \frac{\sqrt{B\pi}}{\Delta T_{nuc}}\,\mathrm{erfc}\left(\frac{\sqrt{B}}{\Delta T_{nuc}}\right)\right] = R$$

which constitutes the working equation for correlating the classical homogeneous nucleation theory with experimentally measured nucleating points expressed as ΔT_{nuc}. The values of B and (A/ρ^*) are varied as fitting parameters, and a least-squares minimization procedure is used to fit nucleation theory ΔT_{nuc} predictions to experimental ΔT_{nuc} points across the cooling rate range 0.5 to 5 °C/min. Correlated values of the surface energy σ derived from the optimized parameter B are shown in Table 2. With correlated values for the variables σ and (A/ρ_n^*), the inverse of the nucleation rate can readily be expressed as a function of the supersaturation ratio in the following linearized form:

$$\ln\left(\frac{\rho_n^*}{J}\right) = \ln\left(\frac{\rho_n^*}{A}\right) + \frac{16\pi\sigma^3\nu^2}{3k^3T^3(\ln S)^2}$$

At constant cooling rate conditions, the maximum nucleation rate, J_{nuc}, is attained at the nucleation point, where the supersaturation ratio is denoted S_{nuc} and the temperature is denoted T_{nuc}. Hence,

$$\ln\left(\frac{\rho_n^*}{J_{nuc}}\right) = \ln\left(\frac{\rho_n^*}{A}\right) + \frac{16\pi\sigma^3\nu^2}{3k^3T_{nuc}^{\,3}(\ln S_{nuc})^2}$$

Figure 5 shows the linearized form of the maximum nucleation rate (for 4% initial paraffin contents) as a function of $1/(\ln S)^2$ and facilitates the appropriate comparison of theoretical and experimental nucleation rates.

Literature Cited

(1) Dirand, M.; Chevallier, V.; Provost, E.; Bouroukba, M.; Petitjean, D. Multicomponent paraffin waxes and petroleum solid deposits: Structural and thermodynamic state. *Fuel* **1998**, *12*, 1253.

(2) Chevallier, V.; Provost, E.; Bourdet, J.B.; Bouroukba, M.; Petitjean, D.; Dirand, M. Mixtures of numerous different *n*-alkanes: 1. Structural Studies by X-ray diffraction at room temperature—Correlation between the crystallographic long c parameter and the average composition of multi-alkane phases. *Polymer* **1999**, *40*, 2121.

(3) Chevallier, V.; Petitjean, D.; Bouroukba, M.; Dirand, M. Mixtures of numerous different *n*-alkanes: 2. Studies by X-ray diffraction and differential thermal analysis with increasing temperature. *Polymer* **1999**, *40*, 2121.

(4) Sirota, E. B.; King, H.E., Jr.; Shao, H.; and Singer, D.M. Rotator phases in mixtures of *n*-alkanes. *J. Chem. Phys.* **1995**, *99*, 798.

(5) Dorset, D. L.; Snyder, R. G. Chain length and the cosolubility of *n*-paraffins in the solid state. *Macromolecules* **1990**, *23*, 623.

(6) Clavell-Grunbaum, D.; Strauss, H. L.; Snyder, R. G. Structure of Model Waxes: Conformational Disorder and Chain Packing in Crystalline Multicomponent *n*-Alkane Solid Solutions. *J. Phys. Chem.* **1997**, *101*, 335.

(7) Srivastava, S. P. ; Handoo, J.; Agrawal, K. M.; Joshi, G. C. Phase transition studies in *n*-alkanes and petroleum-related waxes—A review. *J. Phys. Chem. Solids* **1993**, *6*, 639.

(8) Hammami, A.; Mehrotra, A. Nonisothermal crystallization kinetics of binary mixtures of *n*-alkanes: Ideal eutectic and isomorphous systems. *Fuel* **1996**, *75*, 500.

(9) Taggart, A.; Voogt, F.; Clydesdale, G.; Roberts, K. *Langmuir* **1996**, *12*, 5722.

(10) Kraack, H.; Deutsch, M.; Sirota, E. B. *n*-Alkane Homogeneous Nucleation: Crossover to Polymer Behavior. *Macromolecules* **2000**, *33*, 6174.

(11) Kraack, H.; Sirota, E. B.; Deutsch, M. Measurement of homogeneous nucleation in normal-alkanes. *J. Chem. Phys.* **2000**, *112*, 6873.

(12) Sirota, E. B. Supercooling and transient phase indused nucleation in *n*-alkane solutions. *J. Chem. Phys.* **2000**, *112*, 492.

(13) Chevallier, V.; Bouroukba, M.; Petitjean, D.; Dirand, M.; Pauly, J.; Daridon, J. L.; Ruffier-Meray, V. Crystallization of a multiparaffinic wax in normal tetradecane. *Fuel* **2000**, *79*, 1743.

(14) Coutinho, J. A. P. Predictive local composition models: NRTL and UNIQUAC and their application to model solid−liquid equilibrium of *n*-alkanes. *Fluid Phase Equilib.* **1999**, *159*, 447.

(15) Lira-Galeana, C.; Firoozabadi, A.; Prausnitz, J. M. Thermodynamics of Wax Precipitation in Petroleum Mixtures. *AIChE J.* **1996**, *42*, 239.

(16) Singh, P.; Venkatesan, R.; Fogler, H. S.; Nagarajan, N. Formation and Aging of Incipient Thin Film Wax−Oil Gels. *AIChE J.* **2000**, *46*, 1059.

(17) Singh, P.; Venkatesan, R.; Fogler, H. S.; Nagarajan, N. Morphological Evolution of Thick Wax Deposits during Aging. *AIChE J.* **2001**, *47*, 6.

(18) Singh, P.; Youyen, A.; Fogler, H. S. Existence of a Critical Carbon Number in the Aging of a Wax−Oil Gel. *AIChE J.* **2001**, *9*, 2111.

(19) Venkatesan, R. The Deposition and Rheology of Organic Gels. Ph.D. Thesis, University of Michigan, Ann Arbor, MI, 2004.

(20) Weispfennig, K. Advancements in Paraffin Testing Methodology. *Proceedings of the 2001 SPE International Symposium on Oilfield Chemistry*, Houston, TX, 2001; Paper SPE 64997.

(21) Singh, P.; Fogler, H. S.; Nagarajan, N. Prediction of the Wax Content of the Incipient Wax−Oil Gel in a Pipeline: An Application of the Controlled-Stress Rheometer. *J. Rheol.* **1999**, *43*, 1437.

(22) Venkatesan, R.; Singh, P.; Fogler, H. S. Delineating the Pour Point and Gelation Temperature of Waxy Crude Oils. *SPE J.* **2002**, *Dec*, 349.

(23) Ashbaugh, H. S.; Radulescu, A.; Prud'homme, R. K.; Schwahn, D.; Richter, D.; Fetters, L. J. Interaction of Paraffin Wax Gels with Random Crystalline/Amorphous Hydrocarbon Copolymers. *Macromolecules* **2002**, *35*, 7044.

(24) Mullin, J. W. *Crystallization*, 4th ed.; Butterworth-Heinemann: Oxford, 2001.

(25) Petersen, K. S.; Skovborg, P.; Ronningsen, H. P. Wax Precipitation from North Sea Crude Oils. 4. Thermodynamic Modeling. *Energy Fuels* **1991**, *5*, 924.

(26) Yi, Y.-B.; Sastry, A. M. Analytical approximation of the percolation threshold for overlapping ellipsoids of revolution. *Proc. R. Soc. London, Ser. A* **2004**, *460*, 2353.

(27) Jogun, S. M.; Zukoski, C. F. Rheology and microstructure of dense suspensions of plate-shaped colloidal particles. *J. Rheol.* **1999**, *43*, 847.

(28) Imia, T.; Nakamura, K.; Shibata, M. Relationship between the hardness of an oil−wax gel and the surface structure of the wax crystals. *Colloids Surf., A* **2001**, *194*, 233.

Received for review March 8, 2005
Revised manuscript received June 10, 2005
Accepted June 27, 2005

IE050325U